

1 INTRODUCTION

2 Above Earth's atmosphere are the Van Allen radiation belts, a toroidally-shaped  
3 pair of belts that consist of a complex and dynamic plasma environment. The inner  
4 radiation belt is stable, consists of mostly energetic protons, and is located within 2  
5 Earth radii (measured near the equator) above Earth's surface. The outer radiation  
6 belt, on the other hand, consists of mostly energetic electrons, is highly dynamic  
7 on day and hour time scales, and is typically found between 4 and 8 Earth radii  
8 above Earth's surface. These belts pose a threat to space exploration due to their  
9 adverse effects on our bodies and electrical components. A few **effects** include: a  
10 high radiation dose for manned missions, degradation of silicon that causes transistor  
11 malfunction, computer memory corruption due to bit flips, etc. With these effects in  
12 mind, it is no surprise that the radiation belts have been extensively studied since  
13 their discovery in the 1960s.

14 The radiation belt particles, mostly consisting of electrons and protons, are at  
15 times unstable to wave growth and generate electric and magnetic waves. These  
16 waves can then accelerate and scatter radiation belt particles with a variety of wave-  
17 particle mechanisms. These wave-particle interactions are believed to be responsible  
18 for scattering electron microbursts, a short and intense increase of precipitating  
19 electrons into Earth's atmosphere, that are capable of destroying ozone molecules  
20 and rapidly deplete the outer belt's electrons.

21 Electron microbursts, henceforth referred to as microbursts, are typically  
22 observed by low Earth orbiting spacecraft, sounding rockets, and high altitude  
23 balloons as a sub-second impulse of electrons. Some of the most intense microbursts  
24 have electron fluxes that are a factor of 10 to 100 above the background (for example  
25 see Fig. 7 in Blake et al. (1996)). Since they were first reported by Anderson and

26 Milton (1964), the intense transient nature of microbursts have compelled countless  
27 researchers to pursue an understanding of their properties, their effects on the  
28 environment, and the physical mechanism(s) that create microbursts. Microbursts  
29 are widely believed to be created by wave-particle scattering between a plasma wave  
30 called whistler mode chorus and outer radiation belt electrons, although many details  
31 regarding the scattering mechanism are unconstrained or unknown. The goal of this  
32 dissertation is to expand our knowledge of the wave-particle scattering mechanism  
33 that scatters electron microbursts.

34 This chapter serves as an introduction to the fundamental physical concepts  
35 that are essential to understand wave-particle interactions in Earth's magnetosphere.  
36 We will review the motion of charged particles in electric and magnetic fields, how  
37 particles are organized in the magnetosphere, how particles are accelerated and lost in  
38 the magnetosphere, and review the current state of our understanding of microbursts.

39 Then the rest of this dissertation expands our knowledge of microbursts. In  
40 Chapter ?? (chapter numbers will be filled in the full dissertation) we will investigate  
41 and model the scattering mechanism responsible for microbursts observed inside the  
42 outer radiation belt, near the magnetic equator. Then in Chapters ?? and ?? we  
43 will investigate the microburst scattering mechanism indirectly by estimating the  
44 microburst footprint size in low Earth orbit and the magnetic equator (near where  
45 microburst electrons are believed to be scattered) and compare it to sizes of chorus  
46 waves estimated in prior literature.

47 Charged Particle Motion in Electric and Magnetic Fields

A charged particle trapped in the magnetosphere will experience three types of periodic motion in Earth's nearly dipolar magnetic field in the absence of electric fields. The three motions are ultimately due to the Lorentz force that a particle of

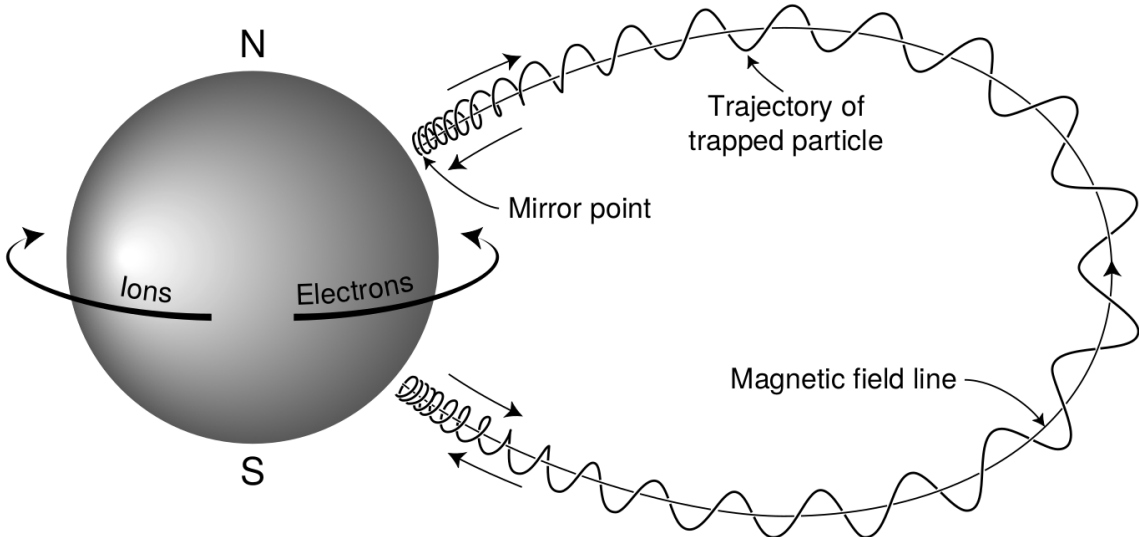


Figure 1.1: The three periodic motions of charged particles in Earth's dipole magnetic field. These motions are: gyration about the magnetic field line, bounce motion between the magnetic poles, and azimuthal drift around the Earth. Figure from (Baumjohann and Treumann, 1997).

momentum  $\vec{p}$ , charge  $q$ , and velocity  $\vec{v}$  experiences in an electric field  $\vec{E}$  and magnetic field  $\vec{B}$  and is given by

$$\frac{d\vec{p}}{dt} = q(\vec{E} + \vec{v} \times \vec{B}). \quad (1.1)$$

- <sup>48</sup> In the magnetosphere, the three periodic motions, in decreasing frequency, are
- <sup>49</sup> gyration, bounce, and drift and are schematically shown in Fig. 1.1. Each periodic
- <sup>50</sup> motion has a corresponding conserved quantity i.e. an adiabatic invariant.

The highest frequency periodic motion is gyration about a magnetic field of magnitude  $B$ . This motion is circular with a Larmor radius of

$$r = \frac{mv_{\perp}}{|q|B} \quad (1.2)$$

where  $m$  is the mass and  $v_{\perp}$  the particle's velocity perpendicular to  $\vec{B}$ . This motion

has a corresponding gyrofrequency of

$$\Omega = \frac{|q|B}{m} \quad (1.3)$$

in units of radians/second. In the radiation belts, the electron gyrofrequency,  $\Omega_e$ , is on the order of a kHz. The corresponding adiabatic invariant is found by integrating the particle's canonical momentum around the particle's path of gyration,

$$J_i = \oint (\vec{p} + q\vec{A}) \cdot d\vec{l} \quad (1.4)$$

where  $J_i$  is the  $i^{th}$  adiabatic invariant and  $\vec{A}$  is the magnetic vector potential. This integral is carried out by integrating the first term over the circumference of the gyro orbit and integrating the second term using Stokes theorem to calculate the magnetic flux enclosed by the gyro orbit. The gyration invariant is  $J_1 \sim v_\perp^2/B$  which is conserved when the frequency,  $\omega$ , of a force acting on the gyrating electron satisfies

$$\omega \ll \Omega_e.$$

The second highest frequency periodic motion is bouncing due to a parallel gradient in  $\vec{B}$ . This periodic motion naturally arises in the magnetosphere because Earth's magnetic field is stronger near the poles. To understand this motion we first we need to define the concept of pitch angle,  $\alpha$  as the angle between  $\vec{B}$  and  $\vec{v}$  which is schematically shown in Fig. 1.2a. The pitch angle relates  $v$  with  $v_\perp$  and  $v_{||}$ , the component of the particles velocity parallel to  $\vec{B}$ . As shown in Fig. 1.2b and 1.2c, a smaller (larger)  $\alpha$  will increase (decrease) the distance that the charged particle travels parallel to  $\vec{B}$  during one gyration.

Assuming the particle's kinetic energy is conserved, the conservation of  $J_1$  implies that given a particle's  $v_\perp(0)$  and  $B(0)$  at the magnetic equator (where Earth's magnetic field is usually at a minimum) we can calculate its  $v_\perp(s)$  along

the particle's path,  $s$ , by calculating  $B(s)$  from magnetic field models. Thus the particle's perpendicular velocity is then related via

$$\frac{v_{\perp}^2(0)}{B(0)} = \frac{v_{\perp}^2(s)}{B(s)} \quad (1.5)$$

<sup>65</sup> which can be rewritten as

$$\frac{v^2 \sin^2 \alpha(0)}{B(0)} = \frac{v^2 - v_{\parallel}^2(s)}{B(s)} \quad (1.6)$$

<sup>66</sup> and re-arranged to solve for  $v_{\parallel}(s)$  by

$$v_{\parallel}(s) = v \sqrt{1 - \frac{B(s)}{B(0)} \sin^2 \alpha(0)} \quad (1.7)$$

<sup>67</sup> which will tend towards 0 as the second term in the radical approaches 1.

<sup>68</sup> The location where  $v_{\parallel}(s) = 0$  is called the mirror point and is where a particle  
<sup>69</sup> reverses direction. Since Earth's magnetic field is stronger towards the poles, the  
<sup>70</sup> mirroring particle will execute periodic bounce motion between its two mirror points  
<sup>71</sup> in the northern and southern hemispheres. The corresponding adiabatic invariant,  $J_2$   
<sup>72</sup> is

$$J_2 = \oint p_{\parallel} ds \quad (1.8)$$

where  $ds$  describes the particle path between the mirror points in the northern and southern hemispheres (see Fig. 1.1).  $J_2$  is found by substituting Eq. 1.7 into Eq. 1.8 and defining the magnetic field strength at the mirror points as  $B_m$  (where  $\alpha(m) = 90^\circ$ ). The  $J_2$  integral can be written as

$$J_2 = 2p \int_{m_n}^{m_s} \sqrt{1 - \frac{B(s)}{B(m)}} ds \quad (1.9)$$

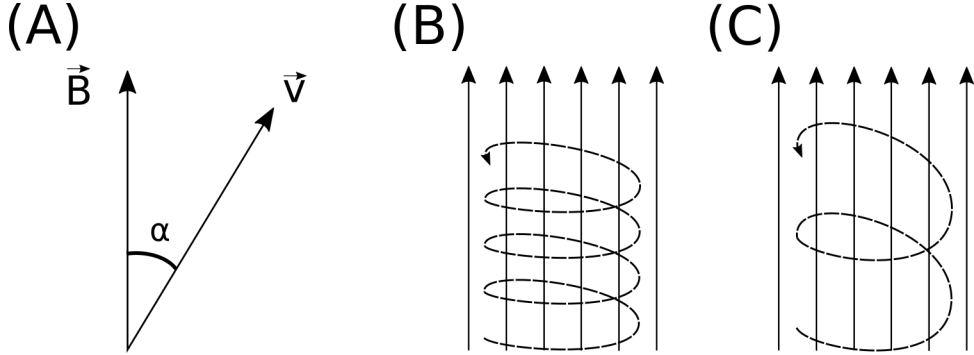


Figure 1.2: Charged particle motion in a uniform magnetic field  $\vec{B}$ . Panel (A) shows the geometry defining the pitch angle,  $\alpha$ . Panel (B) and (C) show two helical electron trajectories with dashed lines assuming a large and small  $\alpha$  (corresponding to a small and large parallel velocity  $v_{||}$ ), respectively.

73 where  $m_n$  and  $m_s$  are the northern and southern mirror points, respectively. The  
 74 bounce period can be estimated (e.g. Baumjohann and Treumann, 1997) to be

$$t_b \approx \frac{LR_e}{\sqrt{W/m}}(3.7 - 1.6 \sin \alpha(0)) \quad (1.10)$$

75 where  $W$  is the particle's kinetic energy, and  $L$  is the  $L$ -shell. The  $L$ -shell is the  
 76 distance from the Earth's center to the location where a particular magnetic field  
 77 line crosses the magnetic equator, in units of Earth radii,  $R_e$ . As with gyration, the  
 78 particle will bounce between the mirror points as long as  $\omega \ll \Omega_b$ , where  $\Omega_b$  is the  
 79 bounce frequency.

80 At this stage it is instructional to introduce loss cone pitch angle,  $\alpha_L$ .  
 81 Conventionally, the loss cone pitch angle is defined as the pitch angle where a particle  
 82 will mirror at  $\approx 100$  km altitude in the atmosphere. A charged particle gyrating at  
 83 those altitudes will encounter and Coulomb scatter with the dense atmosphere and  
 84 be lost. The 100 km altitude is only a convention and not a hard boundary, e.g. the  
 85 peak in the 1 MeV electron ionization rate is at  $\approx 60$  km altitudes (Fang et al., 2010).

86 The slowest periodic motion experienced by charged particles in Earth's

87 magnetic field is azimuthal drift around the Earth. This drift primarily results from  
 88 a combination of a radial gradient in  $\vec{B}$  and the curvature of the magnetic field. The  
 89 radial gradient drift arises because Earth's magnetic field is stronger near the Earth.  
 90 The particle's gyroradius shrinks as it gyrates towards Earth, and expands when it  
 91 gyrates away from Earth. The overall effect is the particle gyro orbit does not close  
 92 on itself causing eastward drift of negatively charged particles and westward drift  
 93 of positively charged particles. The radial gradient drift is further enhanced by the  
 94 centrifugal force that a particle experiences as it bounces along the curved field lines.  
 95 The drift adiabatic invariant,  $J_3$  is found by integrating Eq. 1.4 over the complete  
 96 particle orbit around the Earth. The shape of this drift orbit is known as a drift shell,  
 97 and can be visualized by rotating the trapped particle trajectory in Fig. 1.1 around  
 98 the axis that connects the poles. For  $J_3$ , the first term is negligible and the second  
 99 term is the magnetic flux enclosed by the drift shell,  $\Phi_m$  i.e.  $J_3 \sim \Phi_m$  Add the  $J_3$   
 100 derivation.

101 To quantify the frequencies of the three periodic motions, Fig. 1.3 from Schulz  
 102 and Lanzerotti (1974) shows contours of the gyration, bounce, and drift frequencies  
 103 for electrons and protons in Earth's dipole magnetic field.

Up until now we have considered the three periodic motions due Earth's magnetic field in the absence of electric fields. If there is an electric field,  $\vec{E}$ , perpendicular to  $\vec{B}$ , a particle's center of gyration (averaged position of the particle over a gyration) will drift with a velocity perpendicular to both  $\vec{E}$  and  $\vec{B}$ . The drift velocity can be solved using Eq. 1.1 and is

$$\vec{v}_E = \frac{\vec{E} \times \vec{B}}{B^2}. \quad (1.11)$$

104 If there is a parallel magnetic field,  $E_{||}$ , then the particle is accelerated along the  
 105 magnetic field line. An  $E_{||}$  pointing away from the Earth will contribute to the mirror

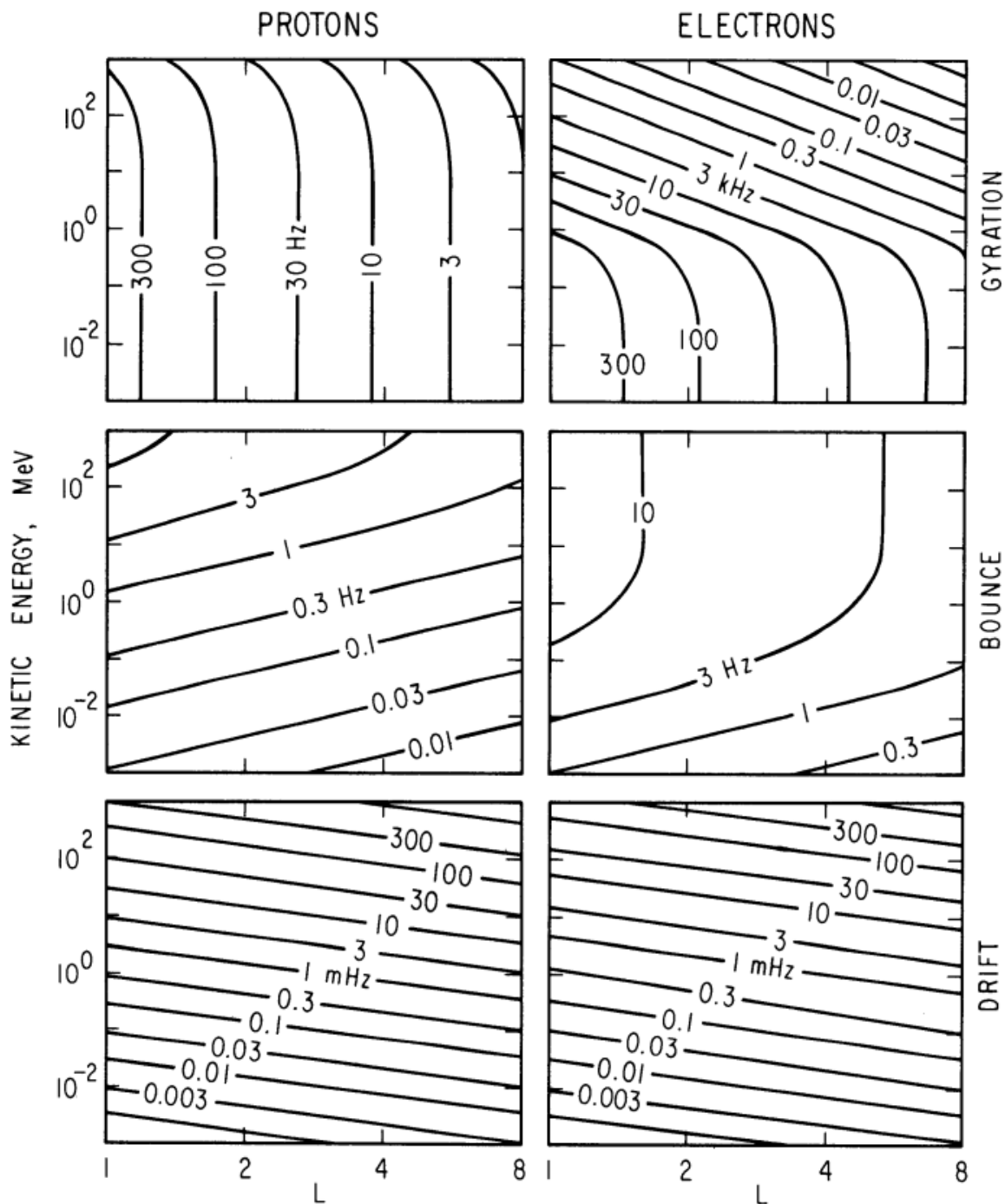


Figure 1.3: Contours of constant gyration, bounce, and drift frequencies for electrons and protons in a dipole field. Figure from Schulz and Lanzerotti (1974).

106 force and raise the particle's mirror point. On the contrary, an Earthward pointing  
 107  $E_{||}$  will oppose the mirror force and lower the mirror point. If the Earthward  $E_{||}$   
 108 lowers the mirror point into the atmosphere, those particles will precipitate into the  
 109 atmosphere. This is the mechanism that generates the aurora.

110 Particle Populations and Their Interractions in the Magnetosphere

111 Now that we have looked at the dynamics of single-particle motion in electric  
 112 and magnetic fields, we will briefly tour the various macroscopic populations in the  
 113 magnetosphere that are illustrated in Fig. 1.4.

114 The sun and its solar wind are ultimately the source of energy input into the  
 115 magnetosphere. The solar wind at Earth's orbit is a plasma traveling at supersonic  
 116 speeds with an embedded interplanetary magnetic field (IMF). When the solar wind  
 117 encounters Earth's magnetic field, the plasma can not easily penetrate into the  
 118 magnetosphere because the plasma is frozen-in on magnetic field lines. The plasma  
 119 is frozen-in on magnetic field lines because plasma has a nearly infinite conductivity.  
 120 Thus the plasma and its magnetic field drapes around the magnetosphere, forming a  
 121 cavity in the solar wind that qualitatively has a shape as shown in Fig. 1.4. The solar  
 122 wind is supersonic at 1 AU so a bow shock exists upstream of the magnetosphere  
 123 which compresses and heats the solar wind. Downstream of the bow shock, the  
 124 solar wind plasma flows around the magnetosphere inside the magnetosheath. The  
 125 magnetopause is the surface where the solar wind ram and Earth's magnetic pressures  
 126 balance. To first order, the magnetopause can be thought of as a boundary between  
 127 the solar wind and Earth's magnetosphere. The shocked plasma then flows past the  
 128 Earth where it shapes the magnetotail. In the magnetotail, the magnetopause exists  
 129 where the solar wind magnetic pressure balances Earth's magnetic field pressure in  
 130 the lobes. The magnetotail extends on the order of 100  $R_E$  downstream of Earth,

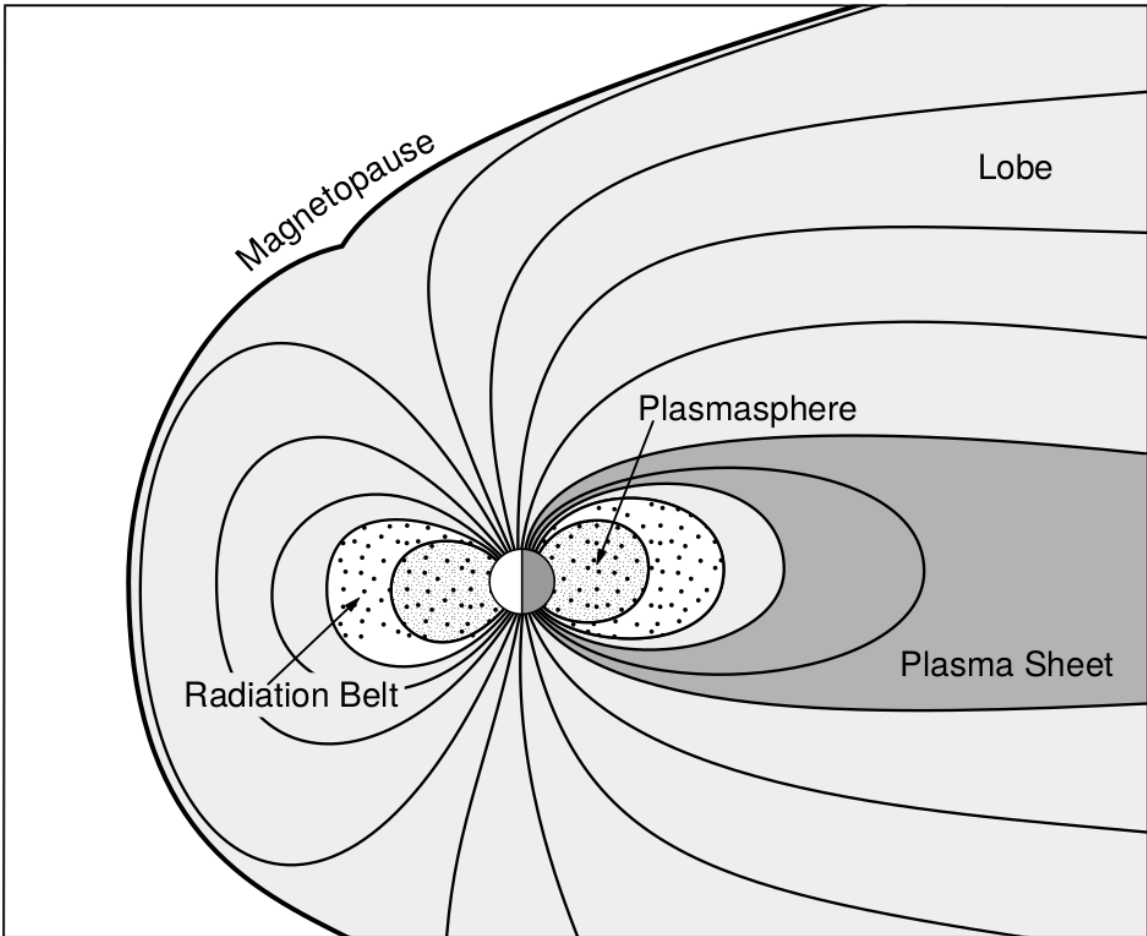


Figure 1.4: A few macroscopic structures in the magnetosphere. The magnetosphere boundary with the solar wind is the magnetopause. The magnetotail consists of two lobes that contain Earth's magnetic flux with the plasma sheet separating the two lobes. The inner magnetosphere contains the plasmasphere, the ring current, and the radiation belts which are co-located. Figure from Baumjohann and Treumann (1997).

and the tailward stretching of magnetic field lines creates a region where Earth's Earthward and anti-Earthward magnetic fields are in proximity. In this region, the curl of  $\vec{B}$  is non-zero, thus by Ampere's law there must be a current (called the plasma sheet) near the magnetic equator (e.g. Eastwood et al., 2015).

### Populations in the Inner Magnetosphere

Closer to Earth, where the magnetic field is largely dipolar, are three plasma populations that comprise the inner magnetosphere: the plasmasphere, the ring current, and the radiation belts which are shown in Fig. 1.4. Before we describe these three particle populations in detail, we will introduce the coordinate system that most naturally describes the inner magnetosphere environment, and the electric fields that mostly effect low energy particles.

In this coordinate system the “radial” coordinate was defined in section 1 and is the L shell. The azimuthal coordinate is the magnetic local time (MLT). For an observer above Earth's north pole looking down, MLT is defined to be 0 (midnight) in the anti-sunward direction and increases in the counter-clockwise direction with 6 at dawn, 12 at noon (sunward direction), and 18 in dusk. The final coordinate is the magnetic latitude,  $\lambda$ , which is analogous to the latitude coordinate in the spherical coordinate system and is defined to be 0 at the magnetic equator. This coordinate system is shown in Fig. 1.5 and naturally describes the inner magnetosphere populations described below.

The low energy particle dynamics in the inner magnetosphere are organized by the co-rotation and the dawn-dusk (pointing from approximately 6 to 18 MLT) electric fields. The co-rotation electric field arises from Earth's rotation. Earth's magnetic field and the particles frozen on it rotate with the Earth so in the magnetosphere (non-rotating) reference frame the particles appear to  $\vec{E} \times \vec{B}$  drift with Earth's

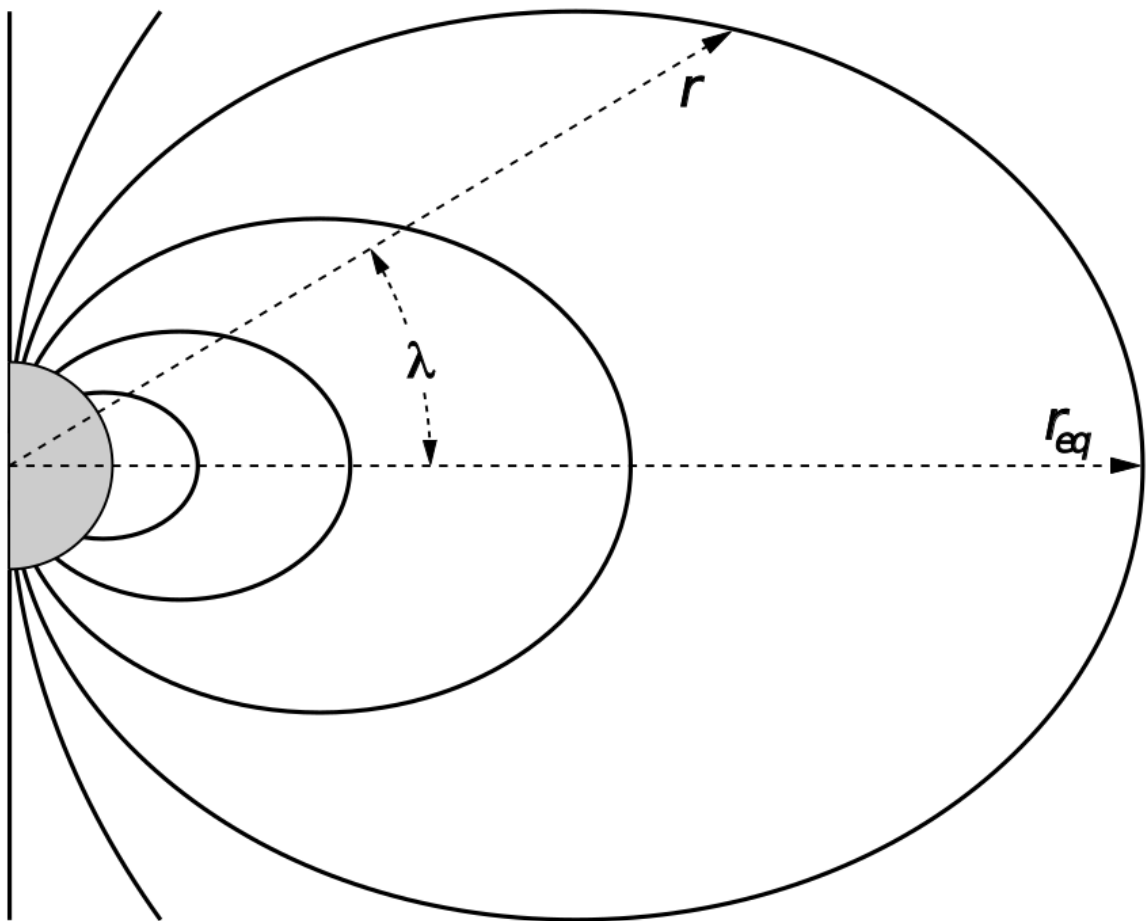


Figure 1.5: The dipole coordinate system. The magnetic latitude of  $\mathbf{r}$  is  $\lambda$ . The radial distance to a magnetic field line in the equatorial plane is typically given by  $L = r_{eq}/R_e$ . Figure from Baumjohann and Treumann (1997).

156 rotation. Make sure the E cross B drift is references correctly. Thus the co-rotation  
 157  $\vec{E}$  points towards Earth. The other electric field points from dawn to dusk is called  
 158 the convection electric field and is due to the Earthward transport of particles from  
 159 the magnetotail. In the magnetosphere reference frame this motion appears as an  
 160 electric field pointing from dawn to dusk. The superposition of the co-rotation and  
 161 and convection electric fields is a potential field shown in Fig. 1.6. The shaded  
 162 area in Fig. 1.6 shows where low energy electrons execute closed orbits around Earth  
 163 (i.e. particles are trapped), and outside this region the particles are not trapped. The  
 164 dynamic topology of the shaded region in Fig. 1.6 is controlled by only the convection  
 165 electric field which is dependent on the solar wind speed and the IMF. Due to  $\vec{E} \times \vec{B}$   
 166 drift, the lowest energy particles orbit along equipotential lines in the shaded region  
 167 in Fig. 1.6 and make up the plasmasphere.

168 Plasmasphere The plasmasphere is relatively dense ( $n_e \sim 10^3/\text{cm}^3$ ), cool ( $\sim \text{eV}$ )  
 169 plasma. The plasmasphere typically extends to  $L \sim 4$  and the spatial extent is  
 170 highly dependent on the solar wind and magnetospheric conditions. The source  
 171 of the plasmasphere is the ionosphere. The two main mechanisms that fill the  
 172 plasmasphere with cold plasma are ionization of the ionosphere by sunlight and  
 173 particle precipitation. The ultraviolet ionization by sunlight is strongly dependent  
 174 on the time of day (day vs night), latitude (more ionization near the equator). The  
 175 ionization due to particle precipitation, on the other hand, is highly dependent on  
 176 magnetospheric conditions, and mostly occurs at high latitudes.

177 The outer boundary of the plasmasphere is the plasmapause which is typically  
 178 identified as a steep radial gradient in plasma density from  $\sim 10^3/\text{cm}^3$  to  $\sim 1/\text{cm}^3$ .  
 179 The location of the plasmapause is important to model (e.g. O'Brien and Moldwin,  
 180 2003) and understand since the plasma density strongly controls the efficiency of

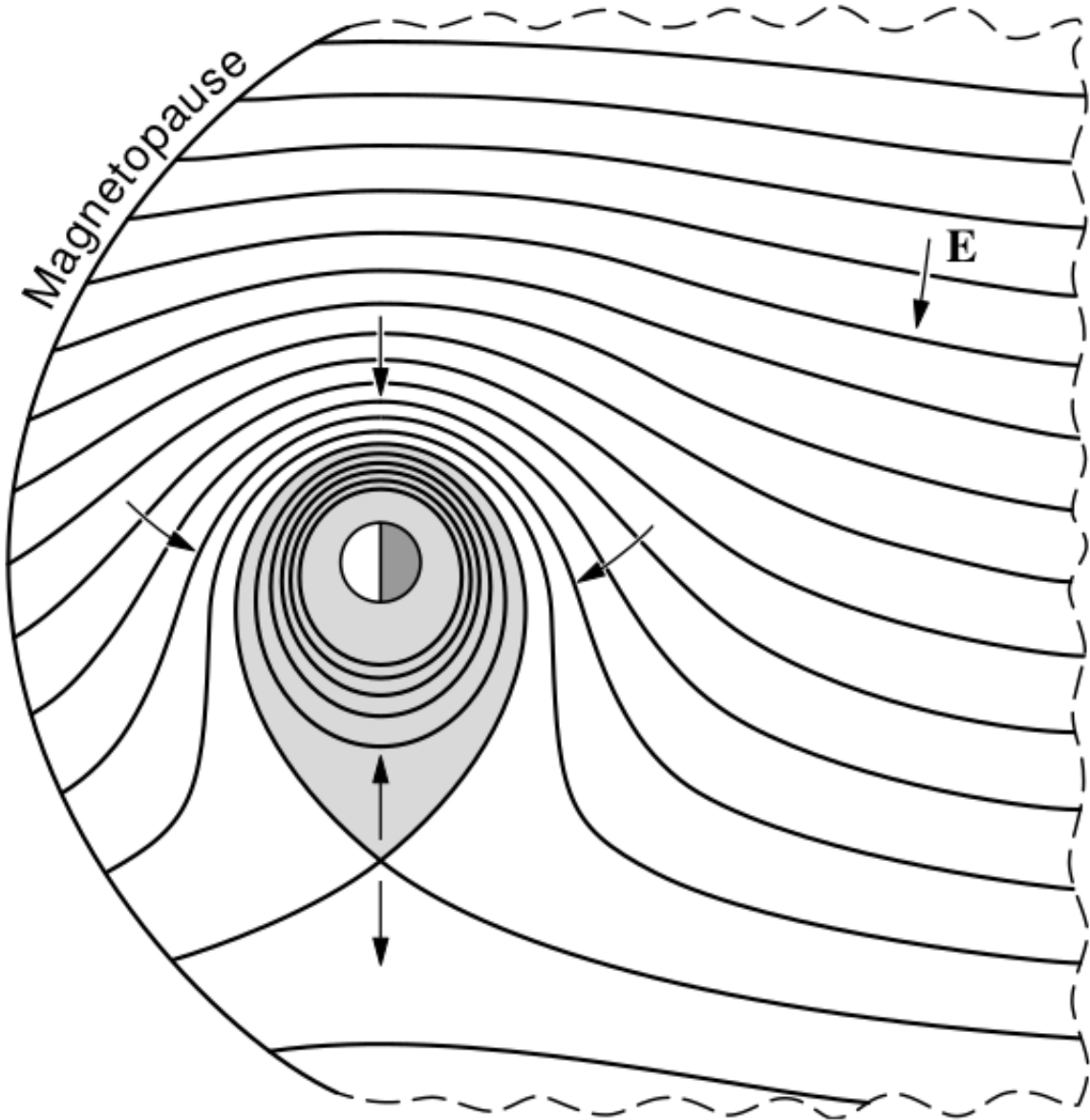


Figure 1.6: Equipotential lines and electric field arrows due to the superposition of the co-rotation and convection electric fields. Electrons in the shaded region execute closed orbits. Outside of the shaded regions the electrons are not trapped and will escape. The region separating the two regimes is called the Alfvén layer. Figure from Baumjohann and Treumann (1997).

<sup>181</sup> particle scattering by waves (e.g. Horne et al., 2005).

<sup>182</sup>        Ring Current The next higher energy population is the ring current. This  
<sup>183</sup> population consists of protons and electrons between tens and a few hundred keV  
<sup>184</sup> that drift around the Earth. The orbits of higher energy particles are not as effected  
<sup>185</sup> by the convection and co-rotation electric field, rather they drift around the Earth  
<sup>186</sup> due to gradient and curvature drifts. Since the direction of the drift is dependent on  
<sup>187</sup> charge, protons drift west around the Earth and electrons drift East. This has the  
<sup>188</sup> effect of creating a current around the Earth.

<sup>189</sup>        The ring current generates a magnetic field which decreases the magnetic field  
<sup>190</sup> strength at the surface of the Earth and increases it outside of the ring current.  
<sup>191</sup> The decrease of Earth's magnetic field strength is readily observed by a system of  
<sup>192</sup> ground-based magnetometers and is merged into a Disturbance Storm Time (DST)  
<sup>193</sup> index to quantify the global reduction in the magnetic field. An example of a DST  
<sup>194</sup> index time series from the 2015 St. Patrick's Day storm, driven by a coronal mass  
<sup>195</sup> ejection (CME), is shown in Fig. 1.7. A few notable features of the storm and the  
<sup>196</sup> ring current are worth pointing out. At the start of the storm the ring current is  
<sup>197</sup> sometimes depleted and DST increases slightly (termed the initial phase or sudden  
<sup>198</sup> storm commencement). Then the ring current population is rapidly built up and  
<sup>199</sup> DST rapidly decreases during the main phase. Lastly, after the storm passes, the  
<sup>200</sup> ring current gradually decays toward its equilibrium state over a period of a few  
<sup>201</sup> days and DST returns towards 0 during the recovery phase. The DST index (along  
<sup>202</sup> with other geomagnetic indices) are readily used by the space physics community to  
<sup>203</sup> quantify the global state of the magnetosphere.

<sup>204</sup>        Radiation Belts The highest particle energy populations are in the Van Allen  
<sup>205</sup> radiation belts. These belts were discovered by Van Allen (1959) and Vernov and

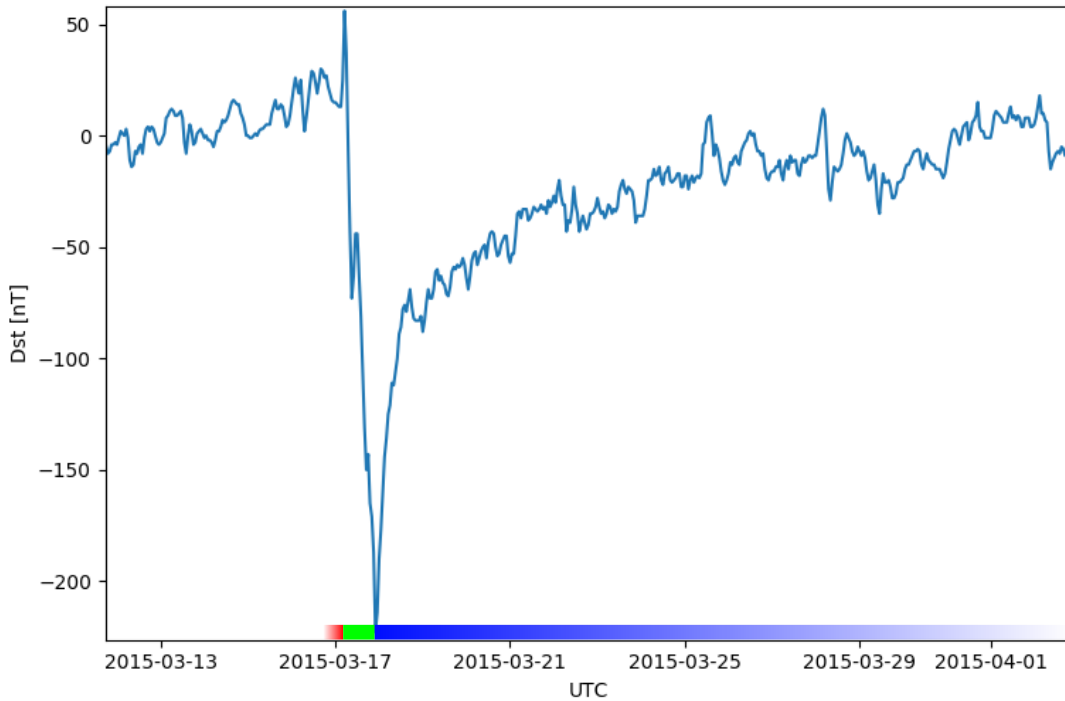


Figure 1.7: The DST index during the St. Patrick's Day 2015 storm. This storm was caused by a coronal mass ejection on March 15th, 2015. The storm phases are: initial phase, main phase, and recovery phase. The initial phase occurred when the Dst peaked at +50 nT on March 17th during which the ring current was eroded by the coronal mass ejection during the interval shown by the red bar shown at the bottom. Then the following rapid decrease to  $\approx -200$  nT was during the main phase where many injections from the magnetotail enhanced the ring current, which reduced Earth's magnetic field strength at the ground, and is shown with the green bar. Lastly, the recovery phase lasted from March 18th to approximately March 29th during which the ring current particles were lost and the ring current returned to its equilibrium state. The recovery phase is shown with the blue bar.

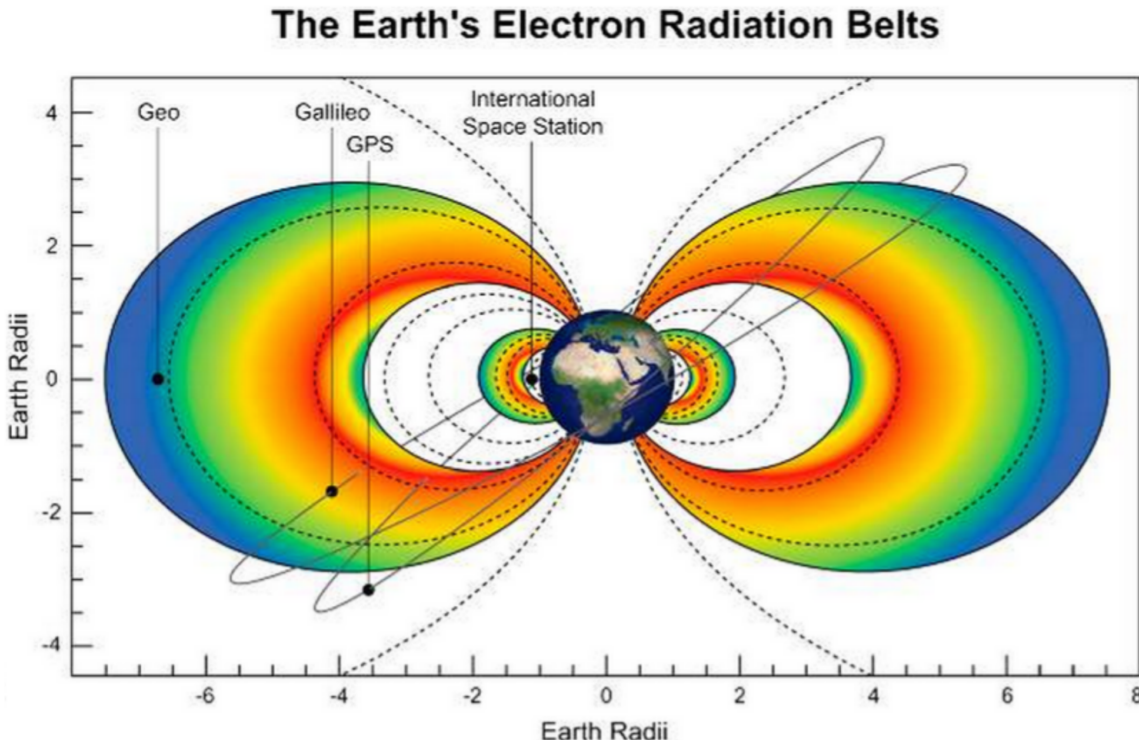


Figure 1.8: The two radiation belts with the locations of various satellites and orbits. Figure from (Horne et al., 2013).

206 Chudakov (1960) during the Cold War and are a pair of toroidally shaped populations  
 207 of trapped electrons and protons shown in Fig. 1.8. Their quiescent toroidal shape,  
 208 similar to the shape of the plasmasphere and ring current, is a result of Earth's dipole  
 209 magnetic field.

210 The inner radiation belt is extremely stable on time periods of years, extends  
 211 to  $L \approx 2$ , and mainly consists of protons with energies between MeV and GeV and  
 212 electrons with energies up to  $\approx 1$  MeV (Claudepierre et al., 2019). The source of  
 213 inner radiation belt protons is believed to be due to cosmic-ray albedo neutron decay  
 214 (e.g. Li et al., 2017) and inward radial diffusion for electrons (e.g. O'Brien et al.,  
 215 2016). The gap between the inner and outer radiation belt is called the slot, which is  
 216 believed to be due to hiss waves inside the plasmasphere (described below) scattering

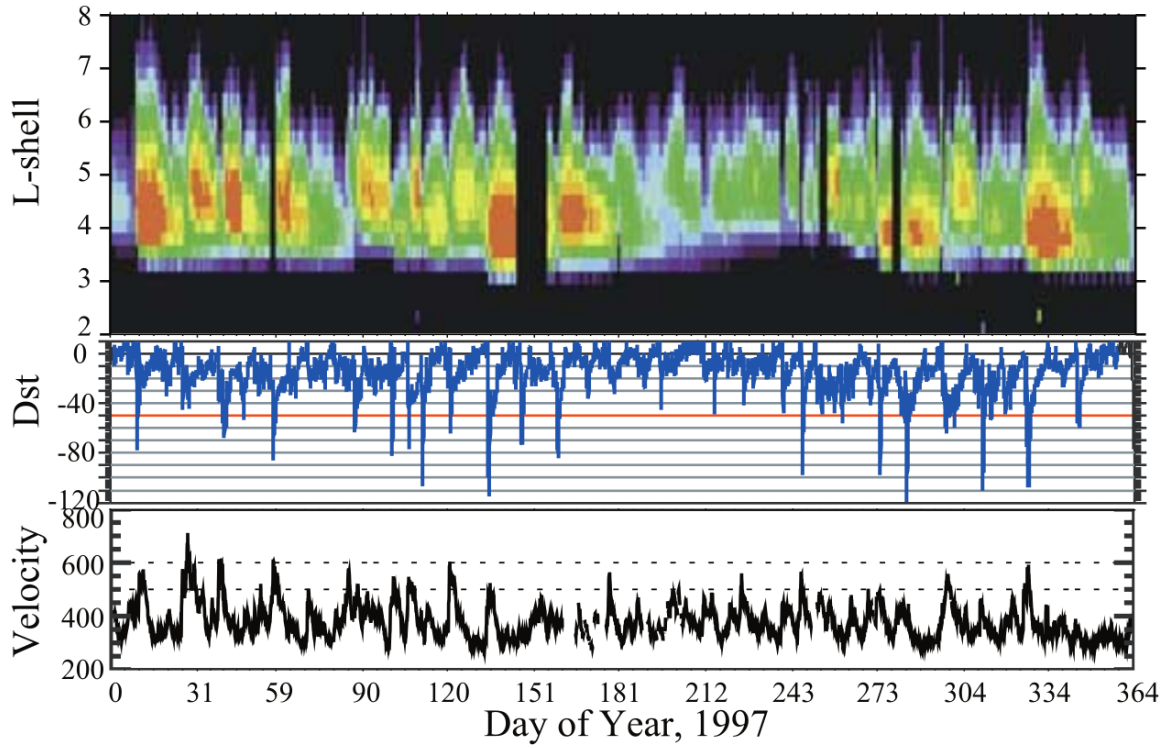


Figure 1.9: The dynamics of the outer radiation belt in 1997 from the POLAR satellite. Top panel shows the 1.2-2.4 MeV electron flux as a function of L and 1997 day of year. The middle panel shows the DST index, and bottom panel shows the solar wind velocity. Figure from (Reeves et al., 2003).

<sup>217</sup> particles into the atmosphere (e.g. Breneman et al., 2015; Lyons and Thorne, 1973).

<sup>218</sup> The outer radiation belt is much more dynamic and consists of mainly electrons  
<sup>219</sup> of energies up to a few MeV. The outer belt's spatial extent is highly variable as  
<sup>220</sup> shown in Fig. 1.9, and is typically observed between L of 4 and 8. The source of  
<sup>221</sup> outer radiation belt electrons is widely believed to be injections of plasma from the  
<sup>222</sup> magnetotail that is then accelerated to high energies.

<sup>223</sup> Due to the highly energetic and dynamic nature of the radiation belts, and their  
<sup>224</sup> impact on human presence in space, the radiation belts have been studied for over  
<sup>225</sup> half century. Researchers have studied and attempted to predict the dynamics of  
<sup>226</sup> radiation belt particles, waves, and wave-particle interactions by considering various  
<sup>227</sup> competing particle acceleration and loss mechanisms which are described next.

<sup>228</sup>

### Radiation Belt Particle Sources and Sinks

<sup>229</sup> Adiabatic Heating

<sup>230</sup> One of the particle heating and transport mechanisms arises from the Earthward  
<sup>231</sup> convection of particles. The conservation of  $J_1$  implies that the initial and final  $v_\perp$   
<sup>232</sup> depends on the change in the magnetic field amplitude

$$\frac{v_{\perp i}^2}{B_i} = \frac{v_{\perp f}^2}{B_f}. \quad (1.12)$$

<sup>233</sup> As a particle convects Earthward,  $B_f > B_i$  thus  $v_\perp$  must increase. The dipole  
<sup>234</sup> magnetic field amplitude can be written as

$$B(L, \theta) = \frac{31.2 \mu\text{T}}{L^3} \sqrt{1 + 3 \cos^2 \theta}. \quad (1.13)$$

<sup>235</sup> The change in  $v_{\perp}^2$  can be found by taking the ratio of  $B(L, \theta)$  at two different  $L$  shells

$$\frac{v_{\perp f}^2}{v_{\perp i}^2} = \left( \frac{L_i}{L_f} \right)^3 \quad (1.14)$$

<sup>236</sup> thus the increase in  $v_{\perp} \sim (L_i/L_f)^{3/2}$ .

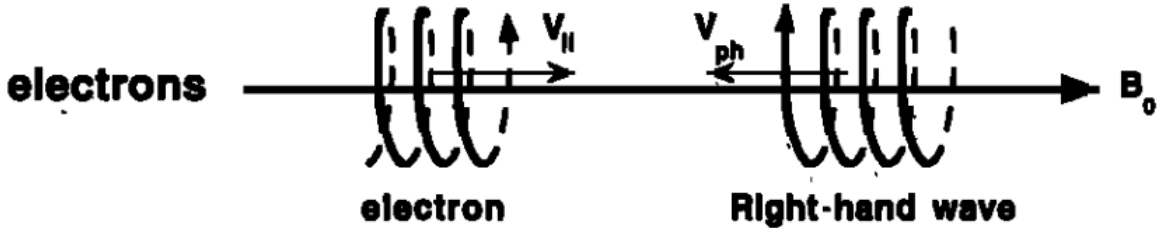
<sup>237</sup> As the particle convects Earthward its  $v_{\parallel}$  also increases because the distance  
<sup>238</sup> between the particle's mirror points decrease. If  $J_2$  is conserved, the shrinking bounce  
<sup>239</sup> path implies that  $v_{\parallel}$  must increase by

$$\frac{v_{\parallel f}^2}{v_{\parallel i}^2} = \left( \frac{L_i}{L_f} \right)^k \quad (1.15)$$

<sup>240</sup> where  $k$  ranges from 2 for equatorial pitch angles,  $\alpha_{eq} = 0^\circ$ , to 2.5 for  $\alpha_{eq} = 90^\circ$   
<sup>241</sup> (Baumjohann and Treumann, 1997). Since the rate of adiabatic heating is greater in  
<sup>242</sup> the perpendicular direction than heating in the parallel direction, an initially isotropic  
<sup>243</sup> particle distribution will become anisotropic during its convection. These isotropic  
<sup>244</sup> particles can then become unstable to wave growth and generate waves in order to  
<sup>245</sup> reach equilibrium.

#### <sup>246</sup> Wave Resonance Heating

<sup>247</sup> Another mechanism that heats particles is due to particles resonating with  
<sup>248</sup> plasma waves. A few of the electromagnetic wave modes responsible for particle  
<sup>249</sup> acceleration (and scattering) relevant to radiation belt dynamics are hiss, whistler  
<sup>250</sup> mode chorus (chorus), and electromagnetic ion cyclotron (EMIC) waves. These waves  
<sup>251</sup> are created by the loss cone instability that is driven by an anisotropy of electrons for  
<sup>252</sup> chorus waves, and protons for EMIC waves. The level of anisotropy can be quantified  
<sup>253</sup> by the ratio of the perpendicular to parallel particle temperatures ( $T_{\perp}/T_{\parallel}$ ). A particle  
<sup>254</sup> distribution is unstable when  $T_{\perp}/T_{\parallel} > 1$ . Since electrons gyrate in a right-handed



$$\omega + k_{\parallel} v_{\parallel} = \Omega^-$$

Figure 1.10: The trajectories of an electron and a right-hand circularly polarized wave during a cyclotron resonance. The electron's  $v_{\parallel}$  and the wave's  $k_{\parallel}$  are in opposite directions such that the wave's frequency is Doppler shifted to an integer multiple of the electron cyclotron frequency. Figure from (Tsurutani and Lakhina, 1997).

255 sense, the chorus waves also tend to be right hand circularly polarized (Tsurutani and  
 256 Lakhina, 1997). The same argument also applies to protons and left hand circularly  
 257 polarized EMIC waves.

258 These circularly polarized waves can resonate with electrons and/or protons  
 259 when their relative motion results in a static  $\vec{E}$ . One example of a resonance between  
 260 a right hand circularly polarized wave and an electron is shown in Fig. 1.10. The  
 261 electron's  $v_{\parallel}$  and the wave's parallel wave vector,  $k_{\parallel}$  are in opposite directions such  
 262 that the wave frequency  $\omega$  is Doppler shifted to an integer multiple of the  $\Omega_e$  where the  
 263 electron feels a static electric field and is accelerated or decelerated. Quantitatively,  
 264 this resonance condition is easier to understand with the following toy model.

265 Assume a uniform magnetic field  $\vec{B} = B_0 \hat{z}$  with a parallel propagating ( $k = k \hat{z}$ ),  
 266 right-hand circularly polarized wave. The wave's electric field as a function of position  
 267 and time can be written as

$$\vec{E} = E_0(\cos(\omega t - kz)\hat{x} + \sin(\omega t - kz)\hat{y}). \quad (1.16)$$

The angular component of  $\vec{E}$  that will effect the particle's  $v_{\perp}$  is

$$E_{\theta} = \vec{E} \cdot \hat{\theta} = E_0 \cos(\omega t - kz + \theta). \quad (1.17)$$

<sup>268</sup> Now assume that the electron is traveling in the  $-\hat{z}$  direction with a velocity  $\vec{v} = -v_0 \hat{z}$

<sup>269</sup> so its time dependent position along  $\hat{z}$  is

$$z(t) = -v_0 t \quad (1.18)$$

<sup>270</sup> and gyrophase is

$$\theta(t) = -\Omega t + \theta(0) \quad (1.19)$$

<sup>271</sup> where the first negative sign comes from the electron's negative charge. Now we put  
<sup>272</sup> this all together and find the force that the electron will experience

$$m \frac{dv_{\theta}}{dt} = qE_{\theta} = qE_0 \sin((\omega + kv_0 - \Omega)t + \theta(0)). \quad (1.20)$$

<sup>273</sup> This is a relatively complex expression, but when the time dependent component is  
<sup>274</sup> 0, i.e.

$$\omega + kv_0 - \Omega = 0, \quad (1.21)$$

<sup>275</sup> the electron will feel a static electric field and be accelerated or decelerated depending  
<sup>276</sup> on  $\theta_0$ , the phase between the wave and the electron. The expression in Eq. 1.21 is  
<sup>277</sup> commonly referred to as the resonance condition and is more generally written as

$$\omega - k_{||} v_{||} = \frac{n\Omega_e}{\gamma} \quad (1.22)$$

278 where  $n$  is the resonance order, and  $\gamma$  is the relativistic correction (e.g. Millan and  
 279 Thorne, 2007). In the case of the cyclotron resonance,  $\omega \approx \Omega_e$  thus  $J_1$  is violated.  
 280 Since  $J_1$  is violated,  $J_2$  and  $J_3$  are also violated since the conditions required to violate  
 281  $J_2$  and  $J_3$  are less stringent than  $J_1$ . It is important to remember that a particle will  
 282 experience the effects of many waves along its drift orbit. The typical MLT extent  
 283 of a handful of waves that are capable of resonating with radiation belt electrons are  
 284 shown in Fig. 1.11.

285 Particle Losses

286 Now that we have seen two general mechanisms with which particles are  
 287 accelerated in the magnetosphere, we will now consider a few specific mechanisms  
 288 that remove particles from the magnetosphere into the atmosphere or the solar  
 289 wind. One mechanism that transports magnetosperic particles into the solar wind  
 290 is magnetopause shadowing (e.g. Ukhorskiy et al., 2006). Magnetopause shadowing  
 291 occurs when the ring current is strengthened and Earth's magnetic field strength is  
 292 increased outside of the ring current. If the ring current increases slowly enough (such  
 293 that  $J_3$  is conserved), a particle drift shell will move outward to conserve  $J_3$ . If the  
 294 particle's drift shell expands past the magnetopause, the particle will be lost to the  
 295 solar wind.

296 **Make sure I understand ULF waves and radial diffusion right** Another particle  
 297 loss (and acceleration) mechanism is driven by ultra low frequency (ULF) waves and  
 298 is called radial diffusion. Radial diffusion is the transport of particles from high  
 299 to low phase space density,  $f$ . If the transport is radially inward, particles will  
 300 appear to be accelerated. On the other hand, radially outward radial diffusion can  
 301 transport particles through the magnetopause where they will be lost to the solar  
 302 wind. Reeves et al. (2013) investigated the driver of particle acceleration during the

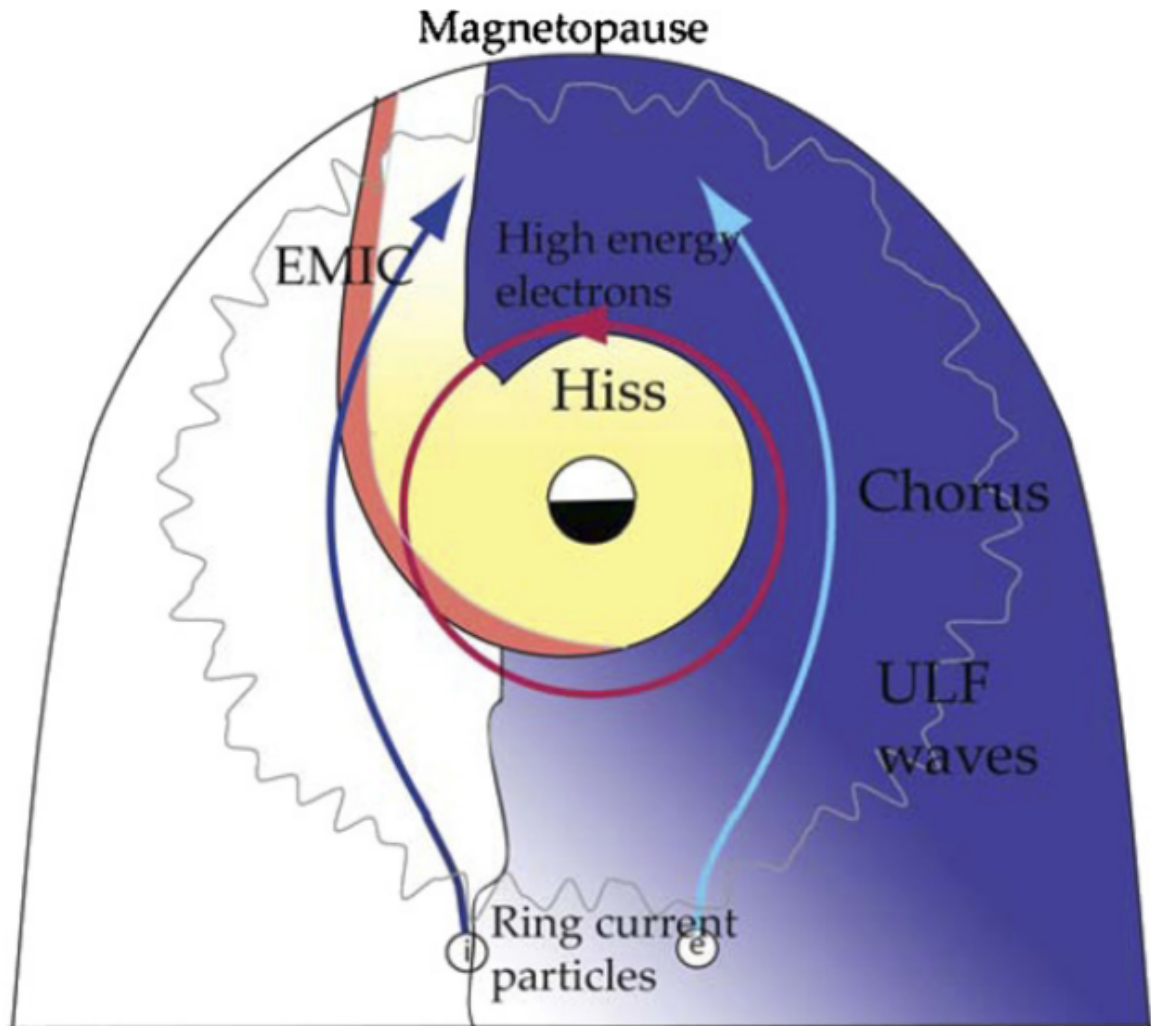


Figure 1.11: Various wave modes in the magnetosphere. Ultra low frequency waves occur through the magnetosphere. Chorus waves are typically observed in the 0-12 midnight-dawn region. EMIC waves are typically observed in the dusk MLT sector. Hiss waves are observed inside the plasmasphere. Figure from Millan and Thorne (2007).

303 October 2012 storm and observationally found that inward radial diffusion was not  
 304 dominant, rather local acceleration via wave-resonance heating appeared to be the  
 305 dominant acceleration mechanism.

306 The loss mechanism central to this dissertation is pitch angle and energy  
 307 scattering of electrons by waves. Some of the waves that scatter electrons in energy  
 308 and pitch angle in the inner magnetosphere are: plasmaspheric hiss (e.g. Breneman  
 309 et al., 2015; O'Brien et al., 2014), EMIC waves (e.g. Capannolo et al., 2019; Hendry  
 310 et al., 2017), and chorus waves (e.g. Breneman et al., 2017; Kasahara et al., 2018;  
 311 Ozaki et al., 2019). These wave-particle interactions occur when the resonance  
 312 condition in Eq. 1.22 is satisfied and the particle's energy and  $\alpha$  is modified by  
 313 the wave. More details regarding the theory of pitch angle and energy diffusion is  
 314 given in Chapter ???. If the wave changes  $\alpha$  towards 0 and  $\alpha < \alpha_L$ , then the particle's  
 315 mirror point dips below 100 km altitude where the particle can be lost from the  
 316 magnetosphere. One manifestation of pitch angle scattering of particles into the loss  
 317 cone are microbursts: a sub-second durtaison impulse of electrons.

318

### Microbursts

319 Microbursts were first with high altitude balloons which measured bremsstrahlung  
 320 X-rays emitted by microburst electrons impacting the atmosphere by Anderson  
 321 and Milton (1964). In the following years, numerous balloon flights expanded our  
 322 knowledge of non-relativistic ( $\leq 500$  keV) microbursts (relativistic microbursts have  
 323 not yet been observed by high altitude balloons) by quantifying the microburst spatial  
 324 extent, temporal width, occurrence frequency, extent in L and MLT, and their source.  
 325 The microburst source was first believed to be either a local plasma instability or a  
 326 propagating disturbance in the magnetosphere (Barcus et al., 1966; Brown et al., 1965;  
 327 Parks, 1967; Trefall et al., 1966). Soon after, both non-relativistic and relativistic

328 microbursts electrons were directly observed in LEO with spacecraft including the  
 329 Solar Anomalous and Magnetospheric Particle Explorer (SAMPEX) (e.g. Blake et al.,  
 330 1996; Blum et al., 2015; Douma et al., 2019, 2017; Greeley et al., 2019; Lorentzen et al.,  
 331 2001a,b; Nakamura et al., 1995, 2000; O'Brien et al., 2004, 2003), Montana State  
 332 University's (MSU) Focused Investigation of Relativistic Electron Bursts: Intensity,  
 333 Range, and Dynamics II (FIREBIRD-II) (Anderson et al., 2017; Breneman et al.,  
 334 2017; Crew et al., 2016; Klumpar et al., 2015; Spence et al., 2012), and Science  
 335 Technologies Satellite (STSAT-I) (e.g. Lee et al., 2012, 2005). An example microburst  
 336 time series is shown in Fig. 1.12 and was observed by the FIREBIRD-II CubeSats.  
 337 The prominent features of the example microbursts in Fig. 1.12 are their sub-second  
 338 duration, half order of magnitude increase in count rate above the falling background,  
 339 and their 200-800 keV energy extent.

340 Microbursts are observed on magnetic field footprints that are connected to the  
 341 outer radiation belt (approximately  $4 < L < 8$ ). They are predominately observed in  
 342 the 0-12 MLT sector with an elevated occurrence frequency during magnetospherically  
 343 disturbed times as shown in Fig. 1.13 (e.g. Douma et al., 2017). O'Brien et al. (2003)  
 344 used SAMPEX relativistic electron data and found that microbursts predominately  
 345 occur during the main phase of storms, with a heightened occurrence rate during the  
 346 recovery phase. Microburst occurrence rates are also higher during high solar wind  
 347 velocity events e.g. from co-rotating interaction regions (Greeley et al., 2019; O'Brien  
 348 et al., 2003).

349 The estimated impact of microbursts on the atmosphere and the radiation  
 350 belts is significant. Relativistic microburst electrons impacting the atmosphere are  
 351 ionized at  $< 100$  km altitudes, with higher energy electrons penetrating closer to  
 352 the surface. The resulting chemical reaction of microburst electrons impacting the  
 353 atmosphere produces odd hydrogen  $\text{HO}_x$  and odd nitrogen  $\text{NO}_x$  molecules, which

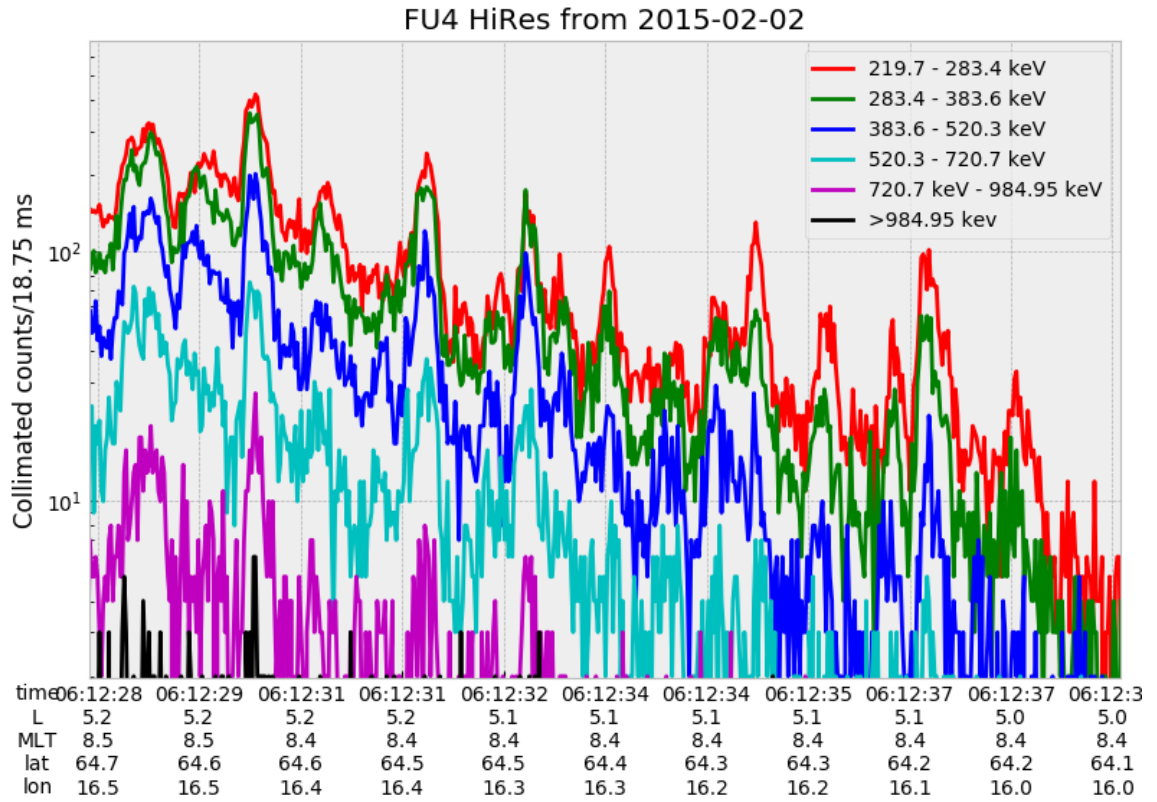


Figure 1.12: An example train of microbursts observed by FIREBIRD-II unit 4 on February 2nd, 2015. The colored curves show the differential energy channel count rates in five channels from  $\approx 200$  keV to 1 MeV and a sixth integral energy channel with a 1 MeV threshold. The x-axis labels show auxiliary information such as time of observation and the spacecraft position in L, MLT, latitude and longitude coordinates.

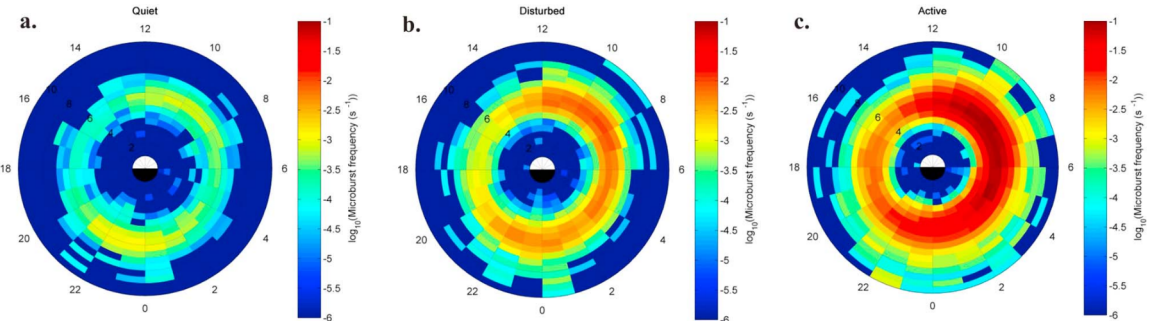


Figure 1.13: Distribution of  $> 1$  MeV microburst occurrence rates as a function of  $L$  and MLT. The three panels show the microburst occurrence rate dependence on geomagnetic activity, parameterized by the auroral electrojet (AE) index for (a)  $AE < 100$  nT, (b)  $100 < AE < 300$  nT and (c)  $AE > 300$  nT. Figure from Douma et al. (2017).

354 are partially responsible for destroying ozone ( $O_3$ ). Seppälä et al. (2018) modeled  
 355 a six hour relativistic microburst storm and found that the mesospheric ozone was  
 356 reduced by  $7 - 12\%$  in the summer months and  $12 - 20\%$  in the winter months, so  
 357 microbursts may have a non-negligible contribution to the dynamics of atmospheric  
 358 ozone. Furthermore, microbursts have also been estimated to have a significant  
 359 impact on the outer radiation belt electron population. Radiation belt electron loss  
 360 due to microbursts has been estimated to be on the order of a day (Breneman  
 361 et al., 2017; Douma et al., 2019; Lorentzen et al., 2001b; O'Brien et al., 2004; Thorne  
 362 et al., 2005).

363 The wave-particle interactions responsible for generating microbursts are also  
 364 believed to accelerate electrons in the radiation belts. As mentioned earlier, when  
 365 an electron is in resonance with a wave, energy is exchanged with the wave and  
 366 the electron is either accelerated or decelerated. The signature of wave-particle  
 367 acceleration been observed for radiation belt electrons (e.g. Horne et al., 2005;  
 368 Meredith et al., 2002; Reeves et al., 2013), and O'Brien et al. (2003) presented evidence  
 369 that enhancements in chorus waves, microbursts, and radiation belt electrons are

370 related. To explain their observations, O'Brien et al. (2003) proposed that microburst  
371 precipitation is a side effect of electron acceleration due to chorus waves.

372 The widely used theoretical framework to model the wave-particle interactions  
373 responsible for accelerating electrons and scattering microbursts is quasi-linear  
374 diffusion (e.g. Horne et al., 2005; Meredith et al., 2002; Summers, 2005; Summers  
375 et al., 1998; Thorne et al., 2005; Walker, 1993). This framework is explained in  
376 Chapter ??, and applied to an observation of a microburst in the heart of the  
377 radiation belt. Qualitatively, when a particle is resonant with a wave it can either  
378 be transported in pitch angle towards the loss cone and lose energy to the wave, or  
379 transported away from the loss cone and gain energy from the wave.

380 As previously mentioned, the range of observed microburst energies range from a  
381 few tens of keV (e.g Datta et al., 1997; Parks, 1967) to greater than 1 MeV (e.g. Blake  
382 et al., 1996; Greeley et al., 2019). The microburst electron flux ( $J$ ) falls off in energy,  
383 and the microburst energy spectra is typically well fit to a decaying exponential

$$J(E) = J_0 e^{-E/E_0} \quad (1.23)$$

384 where  $J_0$  is the flux at 0 keV (unphysical free parameter) and  $E_0$  quantifies the  
385 efficiency of the scattering mechanism in energy (e.g. Datta et al., 1997; Lee et al.,  
386 2005; Parks, 1967). A small  $E_0$  suggests that mostly low energy particles are scattered.  
387 In contrast a high  $E_0$  suggests that the scattering mechanism scatters low and high  
388 energy electrons. Reality is a bit more messy and a high  $E_0$  may be a signature of  
389 a scattering mechanism preferential to high energy electrons, but is hidden by the  
390 convolution of the source particles available to be scattered (typically with a falling  
391 energy spectrum) and the energy-dependent efficiency of the scattering mechanism.

392 The short microburst duration observed by a single LEO satellite has an

393 ambiguity when interpreting what is exactly a microburst. The two possible realities  
 394 are: a microburst is very small and spatially stationary so that the LEO spacecraft  
 395 passes through it in less than a second. Alternatively, microbursts are spatially large  
 396 and transient so a microburst will pass by the spacecraft in a fraction of a second.  
 397 There are a few ways to distinguish between the two possible realities, and each one  
 398 has a unique set of advantages.

399 A high altitude balloon provides essentially a stationary view of the precipitating  
 400 particles under the radiation belt footprints. A short-lived, temporal microburst can  
 401 be unambiguously identified. Spatial structures, on the other hand, are difficult to  
 402 identify because a balloon is essentially still on drift timescales.

403 Multi-spacecraft missions are an alternate solution that can determine if a  
 404 microburst is spatial or temporal. As will be shown in this dissertation, if a microburst  
 405 is observed simultaneously by two spacecraft then it is temporal and has a size  
 406 greater than the spacecraft separation. On the contrary, if two spacecraft observe  
 407 a microburst-like feature at different times but at the same location, then the feature  
 408 is spatial and may be a curtain (Blake and O'Brien, 2016). Both balloon and multi-  
 409 spacecraft observational methods have a unique set of strengths, and this dissertation  
 410 takes the multi-spacecraft approach to identify and study microbursts.

411

### Scope of Reserach

412 This dissertation furthers our understanding of the microburst scattering  
 413 mechanism by presenting observational evidence of microburst scattering directly, and  
 414 measuring microburst sizes and comparing them to the size of chorus waves. Chapter  
 415 ?? describes a microburst scattering event observed by NASA's Van Allen Probes.  
 416 For this event, particle and wave measurements were analyzed and modeled in the  
 417 theoretical framework of pitch angle and energy diffusion. Then the following two

418 chapters present studies of microburst sizes in comparison to chorus waves. Chapter  
419 ?? describes a bouncing packet microburst observation made by the FIREBIRD-II  
420 mission where the microburst's lower bound longitudinal and latitudinal sizes were  
421 estimated. Then Chapter ?? expands the case study from Chapter ?? to a statistical  
422 study of microburst sizes using The Aerospace Corporation's AeroCube-6 (AC6)  
423 CubeSats. In this study, a Monte Carlo and analytic microburst size models were  
424 developed to account for the compounding statistical effects of random microburst  
425 sizes and locations. Lastly, Chapter ?? will summarize this work and make concluding  
426 remarks regarding outstanding questions in microburst physics.

## Bibliography

- 427     Anderson, B., Shekhar, S., Millan, R., Crew, A., Spence, H., Klumpar, D., Blake, J.,  
 429     O'Brien, T., and Turner, D. (2017). Spatial scale and duration of one microburst  
 430     region on 13 August 2015. *Journal of Geophysical Research: Space Physics*.
- 431     Anderson, K. A. and Milton, D. W. (1964). Balloon observations of X rays in the  
 432     auroral zone: 3. High time resolution studies. *Journal of Geophysical Research*,  
 433     69(21):4457–4479.
- 434     Barcus, J., Brown, R., and Rosenberg, T. (1966). Spatial and temporal character of  
 435     fast variations in auroral-zone x rays. *Journal of Geophysical Research*, 71(1):125–  
 436     141.
- 437     Baumjohann, W. and Treumann, R. A. (1997). *Basic space plasma physics*. World  
 438     Scientific.
- 439     Blake, J.,Looper, M., Baker, D., Nakamura, R., Klecker, B., and Hovestadt, D.  
 440     (1996). New high temporal and spatial resolution measurements by sampex of the  
 441     precipitation of relativistic electrons. *Advances in Space Research*, 18(8):171 – 186.
- 442     Blake, J. B. and O'Brien, T. P. (2016). Observations of small-scale latitudinal  
 443     structure in energetic electron precipitation. *Journal of Geophysical Research: Space  
 444     Physics*, 121(4):3031–3035. 2015JA021815.
- 445     Blum, L., Li, X., and Denton, M. (2015). Rapid MeV electron precipitation as  
 446     observed by SAMPEX/HILT during high-speed stream-driven storms. *Journal of  
 447     Geophysical Research: Space Physics*, 120(5):3783–3794. 2014JA020633.
- 448     Breneman, A., Crew, A., Sample, J., Klumpar, D., Johnson, A., Agapitov, O.,  
 449     Shumko, M., Turner, D., Santolik, O., Wygant, J., et al. (2017). Observations  
 450     directly linking relativistic electron microbursts to whistler mode chorus: Van allen  
 451     probes and FIREBIRD II. *Geophysical Research Letters*.
- 452     Breneman, A. W., Halford, A., Millan, R., McCarthy, M., Fennell, J., Sample, J.,  
 453     Woodger, L., Hospodarsky, G., Wygant, J. R., Cattell, C. A., et al. (2015). Global-  
 454     scale coherence modulation of radiation-belt electron loss from plasmaspheric hiss.  
 455     *Nature*, 523(7559):193.
- 456     Brown, R., Barcus, J., and Parsons, N. (1965). Balloon observations of auroral zone  
 457     x rays in conjugate regions. 2. microbursts and pulsations. *Journal of Geophysical  
 458     Research (U.S.)*.
- 459     Capannolo, L., Li, W., Ma, Q., Shen, X.-C., Zhang, X.-J., Redmon, R., Rodriguez,  
 460     J., Engebretson, M., Kletzing, C., Kurth, W., et al. (2019). Energetic electron  
 461     precipitation: multi-event analysis of its spatial extent during emic wave activity.  
 462     *Journal of Geophysical Research: Space Physics*.

- 463 Claudepierre, S., O'Brien, T.,Looper, M., Blake, J., Fennell, J., Roeder, J.,  
 464 Clemmons, J., Mazur, J., Turner, D., Reeves, G., et al. (2019). A revised look  
 465 at relativistic electrons in the earth's inner radiation zone and slot region. *Journal*  
 466 *of Geophysical Research: Space Physics*, 124(2):934–951.
- 467 Crew, A. B., Spence, H. E., Blake, J. B., Klumpar, D. M., Larsen, B. A., O'Brien,  
 468 T. P., Driscoll, S., Handley, M., Legere, J., Longworth, S., Mashburn, K.,  
 469 Mosleh, E., Ryhajlo, N., Smith, S., Springer, L., and Widholm, M. (2016). First  
 470 multipoint in situ observations of electron microbursts: Initial results from the  
 471 NSF FIREBIRD II mission. *Journal of Geophysical Research: Space Physics*,  
 472 121(6):5272–5283. 2016JA022485.
- 473 Datta, S., Skoug, R., McCarthy, M., and Parks, G. (1997). Modeling of microburst  
 474 electron precipitation using pitch angle diffusion theory. *Journal of Geophysical*  
 475 *Research: Space Physics*, 102(A8):17325–17333.
- 476 Douma, E., Rodger, C., Blum, L., O'Brien, T., Clilverd, M., and Blake, J. (2019).  
 477 Characteristics of relativistic microburst intensity from sampex observations.  
 478 *Journal of Geophysical Research: Space Physics*.
- 479 Douma, E., Rodger, C. J., Blum, L. W., and Clilverd, M. A. (2017). Occurrence  
 480 characteristics of relativistic electron microbursts from SAMPEX observations.  
 481 *Journal of Geophysical Research: Space Physics*, 122(8):8096–8107. 2017JA024067.
- 482 Eastwood, J., Hietala, H., Toth, G., Phan, T., and Fujimoto, M. (2015). What  
 483 controls the structure and dynamics of earths magnetosphere? *Space Science*  
 484 *Reviews*, 188(1-4):251–286.
- 485 Fang, X., Randall, C. E., Lummerzheim, D., Wang, W., Lu, G., Solomon, S. C., and  
 486 Frahm, R. A. (2010). Parameterization of monoenergetic electron impact ionization.  
 487 *Geophysical Research Letters*, 37(22).
- 488 Greeley, A., Kanekal, S., Baker, D., Klecker, B., and Schiller, Q. (2019). Quantifying  
 489 the contribution of microbursts to global electron loss in the radiation belts. *Journal*  
 490 *of Geophysical Research: Space Physics*.
- 491 Hendry, A. T., Rodger, C. J., and Clilverd, M. A. (2017). Evidence of sub-mev  
 492 emic-driven electron precipitation. *Geophysical Research Letters*, 44(3):1210–1218.
- 493 Horne, R., Glauert, S., Meredith, N., Boscher, D., Maget, V., Heynderickx, D., and  
 494 Pitchford, D. (2013). Space weather impacts on satellites and forecasting the earth's  
 495 electron radiation belts with spacecast. *Space Weather*, 11(4):169–186.
- 496 Horne, R. B., Thorne, R. M., Shprits, Y. Y., Meredith, N. P., Glauert, S. A., Smith,  
 497 A. J., Kanekal, S. G., Baker, D. N., Engebretson, M. J., Posch, J. L., et al.  
 498 (2005). Wave acceleration of electrons in the van allen radiation belts. *Nature*,  
 499 437(7056):227.

- 500 Kasahara, S., Miyoshi, Y., Yokota, S., Mitani, T., Kasahara, Y., Matsuda, S.,  
 501 Kumamoto, A., Matsuoka, A., Kazama, Y., Frey, H., et al. (2018). Pulsating  
 502 aurora from electron scattering by chorus waves. *Nature*, 554(7692):337.
- 503 Klumpar, D., Springer, L., Mosleh, E., Mashburn, K., Berardinelli, S., Gunderson,  
 504 A., Handly, M., Ryhajlo, N., Spence, H., Smith, S., Legere, J., Widholm, M.,  
 505 Longworth, S., Crew, A., Larsen, B., Blake, J., and Walmsley, N. (2015). Flight  
 506 system technologies enabling the twin-cubesat firebird-ii scientific mission.
- 507 Lee, J. J., Parks, G. K., Lee, E., Tsurutani, B. T., Hwang, J., Cho, K. S., Kim, K.-H.,  
 508 Park, Y. D., Min, K. W., and McCarthy, M. P. (2012). Anisotropic pitch angle  
 509 distribution of 100 keV microburst electrons in the loss cone: measurements from  
 510 STSAT-1. *Annales Geophysicae*, 30(11):1567–1573.
- 511 Lee, J.-J., Parks, G. K., Min, K. W., Kim, H. J., Park, J., Hwang, J., McCarthy,  
 512 M. P., Lee, E., Ryu, K. S., Lim, J. T., Sim, E. S., Lee, H. W., Kang, K. I., and  
 513 Park, H. Y. (2005). Energy spectra of 170–360 keV electron microbursts measured  
 514 by the korean STSAT-1. *Geophysical Research Letters*, 32(13). L13106.
- 515 Li, X., Selesnick, R., Schiller, Q., Zhang, K., Zhao, H., Baker, D. N., and Temerin,  
 516 M. A. (2017). Measurement of electrons from albedo neutron decay and neutron  
 517 density in near-earth space. *Nature*, 552(7685):382.
- 518 Lorentzen, K. R., Blake, J. B., Inan, U. S., and Bortnik, J. (2001a). Observations  
 519 of relativistic electron microbursts in association with VLF chorus. *Journal of  
 520 Geophysical Research: Space Physics*, 106(A4):6017–6027.
- 521 Lorentzen, K. R., Looper, M. D., and Blake, J. B. (2001b). Relativistic electron  
 522 microbursts during the GEM storms. *Geophysical Research Letters*, 28(13):2573–  
 523 2576.
- 524 Lyons, L. R. and Thorne, R. M. (1973). Equilibrium structure of radiation belt  
 525 electrons. *Journal of Geophysical Research*, 78(13):2142–2149.
- 526 Meredith, N., Horne, R., Summers, D., Thorne, R., Iles, R., Heynderickx, D., and  
 527 Anderson, R. (2002). Evidence for acceleration of outer zone electrons to relativistic  
 528 energies by whistler mode chorus. In *Annales Geophysicae*, volume 20, pages 967–  
 529 979.
- 530 Millan, R. and Thorne, R. (2007). Review of radiation belt relativistic electron losses.  
 531 *Journal of Atmospheric and Solar-Terrestrial Physics*, 69(3):362 – 377.
- 532 Nakamura, R., Baker, D. N., Blake, J. B., Kanekal, S., Klecker, B., and Hovestadt,  
 533 D. (1995). Relativistic electron precipitation enhancements near the outer edge of  
 534 the radiation belt. *Geophysical Research Letters*, 22(9):1129–1132.

- 535 Nakamura, R., Isowa, M., Kamide, Y., Baker, D., Blake, J., and Looper, M. (2000).  
 536 Observations of relativistic electron microbursts in association with VLF chorus.  
 537 *J. Geophys. Res.*, 105:15875–15885.
- 538 O'Brien, T., Claudepierre, S., Blake, J., Fennell, J. F., Clemmons, J., Roeder, J.,  
 539 Spence, H. E., Reeves, G., and Baker, D. (2014). An empirically observed pitch-  
 540 angle diffusion eigenmode in the earth's electron belt near  $l^*= 5.0$ . *Geophysical*  
 541 *Research Letters*, 41(2):251–258.
- 542 O'Brien, T., Claudepierre, S., Guild, T., Fennell, J., Turner, D., Blake, J., Clemmons,  
 543 J., and Roeder, J. (2016). Inner zone and slot electron radial diffusion revisited.  
 544 *Geophysical Research Letters*, 43(14):7301–7310.
- 545 O'Brien, T. and Moldwin, M. (2003). Empirical plasmapause models from magnetic  
 546 indices. *Geophysical Research Letters*, 30(4).
- 547 O'Brien, T. P., Looper, M. D., and Blake, J. B. (2004). Quantification of relativistic  
 548 electron microburst losses during the GEM storms. *Geophysical Research Letters*,  
 549 31(4). L04802.
- 550 O'Brien, T. P., Lorentzen, K. R., Mann, I. R., Meredith, N. P., Blake, J. B., Fennell,  
 551 J. F., Looper, M. D., Milling, D. K., and Anderson, R. R. (2003). Energization of  
 552 relativistic electrons in the presence of ULF power and MeV microbursts: Evidence  
 553 for dual ULF and VLF acceleration. *Journal of Geophysical Research: Space*  
 554 *Physics*, 108(A8).
- 555 Ozaki, M., Miyoshi, Y., Shiokawa, K., Hosokawa, K., Oyama, S.-i., Kataoka, R.,  
 556 Ebihara, Y., Ogawa, Y., Kasahara, Y., Yagitani, S., et al. (2019). Visualization of  
 557 rapid electron precipitation via chorus element wave–particle interactions. *Nature*  
 558 *communications*, 10(1):257.
- 559 Parks, G. K. (1967). Spatial characteristics of auroral-zone X-ray microbursts. *Journal*  
 560 *of Geophysical Research*, 72(1):215–226.
- 561 Reeves, G., Spence, H. E., Henderson, M., Morley, S., Friedel, R., Funsten, H., Baker,  
 562 D., Kanekal, S., Blake, J., Fennell, J., et al. (2013). Electron acceleration in the  
 563 heart of the van allen radiation belts. *Science*, 341(6149):991–994.
- 564 Reeves, G. D., McAdams, K. L., Friedel, R. H. W., and O'Brien, T. P. (2003). Ac-  
 565 celeration and loss of relativistic electrons during geomagnetic storms. *Geophysical*  
 566 *Research Letters*, 30(10):n/a–n/a. 1529.
- 567 Schulz, M. and Lanzerotti, L. J. (1974). *Particle Diffusion in the Radiation Belts*.  
 568 Springer.

- 569 Seppälä, A., Douma, E., Rodger, C., Verronen, P., Clilverd, M. A., and Bortnik, J.  
 570 (2018). Relativistic electron microburst events: Modeling the atmospheric impact.  
 571 *Geophysical Research Letters*, 45(2):1141–1147.
- 572 Spence, H. E., Blake, J. B., Crew, A. B., Driscoll, S., Klumpar, D. M., Larsen,  
 573 B. A., Legere, J., Longworth, S., Mosleh, E., O'Brien, T. P., Smith, S., Springer,  
 574 L., and Widholm, M. (2012). Focusing on size and energy dependence of electron  
 575 microbursts from the van allen radiation belts. *Space Weather*, 10(11).
- 576 Summers, D. (2005). Quasi-linear diffusion coefficients for field-aligned electro-  
 577 magnetic waves with applications to the magnetosphere. *Journal of Geophysical  
 578 Research: Space Physics*, 110(A8):n/a–n/a. A08213.
- 579 Summers, D., Thorne, R. M., and Xiao, F. (1998). Relativistic theory of wave-particle  
 580 resonant diffusion with application to electron acceleration in the magnetosphere.  
 581 *Journal of Geophysical Research: Space Physics*, 103(A9):20487–20500.
- 582 Thorne, R. M., O'Brien, T. P., Shprits, Y. Y., Summers, D., and Horne, R. B. (2005).  
 583 Timescale for MeV electron microburst loss during geomagnetic storms. *Journal  
 584 of Geophysical Research: Space Physics*, 110(A9). A09202.
- 585 Trefall, H., Bjordal, J., Ullaland, S., and Stadsnes, J. (1966). On the extension of  
 586 auroral-zone x-ray microbursts. *Journal of Atmospheric and Terrestrial Physics*,  
 587 28(2):225–233.
- 588 Tsurutani, B. T. and Lakhina, G. S. (1997). Some basic concepts of wave-particle  
 589 interactions in collisionless plasmas. *Reviews of Geophysics*, 35(4):491–501.
- 590 Ukhorskiy, A. Y., Anderson, B. J., Brandt, P. C., and Tsyganenko, N. A. (2006).  
 591 Storm time evolution of the outer radiation belt: Transport and losses. *Journal of  
 592 Geophysical Research: Space Physics*, 111(A11):n/a–n/a. A11S03.
- 593 Van Allen, J. A. (1959). The geomagnetically trapped corpuscular radiation. *Journal  
 594 of Geophysical Research*, 64(11):1683–1689.
- 595 Vernov, S. and Chudakov, A. (1960). Investigation of radiation in outer space. In  
 596 *International Cosmic Ray Conference*, volume 3, page 19.
- 597 Walker, A. D. M. (1993). *Plasma waves in the magnetosphere*, volume 24. Springer  
 598 Science & Business Media.